Journal of Computational Physics 399 (2019) 108919

Contents lists available at ScienceDirect

Journal of Computational Physics

www.elsevier.com/locate/jcp

A New method for computing particle collisions in Navier-Stokes flows

Acmae El. Yacoubi [a], Sheng Xu [b], Z. Jane Wang [a,c,*]

[a] Department of Mechanical & Aerospace Engineering, Cornell University, Ithaca NY, 14853, USA
[b] Department of Mathematics, Southern Methodist University, Dallas, TX 75275-0156, USA
[c] Department of Physics, Cornell University, Ithaca NY, 14853, USA

ARTICLE INFO

Article history:
Received 10 June 2018
Received in revised form 16 August 2019
Accepted 29 August 2019
Available online 3 September 2019

Keywords:
Immersed interface method
Particle collisions in fluids
Lubrication theory

ABSTRACT

Particle collisions in fluids are ubiquitous, but to compute the collision dynamics in a Navier-Stokes flow remains challenging. In addition to capturing the two-way coupling between the fluid and the particles, a key difficulty is to resolve the collision dynamics mediated by the flow. The gap between particles during collision is minuscule. This introduces a small length scale which needs to be resolved simultaneously with the flow at the large scale. Our goal is to develop a numerical scheme that is accurate and efficient in computing the Navier-Stokes flow around moving particles while taking into account the effect of the lubrication forces on the collisions. Our method integrates the immersed interface method with the lubrication theory in a way that directly couples all three parts, the bulk flow, the flow in the gap, and the dynamics of the freely moving particles. We present a general algorithm for computing the collision. To test the method, we study four fundamental cases involving normal and tangential collisions, so that we can compare numerics against analytic solutions in the lubrication layer. In addition, we provide the lubrication solution needed for computing collisions between surfaces of any shapes in arbitrary relative motions, so that the method can be applied to other cases.

© 2019 Elsevier Inc. All rights reserved.

1. Introduction

Particle collisions in fluids are ubiquitous and are fundamental to phenomena ranging from sand dune formation to sedimentation in oceans. Understanding the essential physics about particle interactions mediated by a flow requires both laboratory experiments and direct simulations. Compared to experiments, an advantage of using direct numerical simulations is to quantify the entire flow field together with the dynamics of individual particles. However, resolving this coupled system of freely moving particles and an unsteady flow poses computational challenges. One challenge is to resolve the dynamic coupling between the flow and each particle. It requires the correct implementation of the boundary conditions and also the ability to track the moving interfaces accurately. The computation also needs to resolve simultaneously the low Reynolds number flow in the small gaps between the particles and the much higher Reynolds number flow in the bulk.

Freely moving particles in a flow have a strong tendency to cluster. When the particles cluster, the interstitial layers can be much smaller than the grid resolution used for computing the bulk flow. The brute-force grid refinement to resolve the thin layers of the fluid is expensive and is insufficient to resolve the asymptotic behavior of the collision dynamics [2]. For

* Corresponding author at: Department of Mechanical & Aerospace Engineering & Department of Physics, Cornell University, Ithaca NY, 14853, USA.
E-mail address: jane.wang@cornell.edu (Z.J. Wang).

https://doi.org/10.1016/j.jcp.2019.108919
0021-9991/© 2019 Elsevier Inc. All rights reserved.

a quick fix, many studies have introduced ad-hoc collision rules to bypass the treatment of the physics of collisions. These rules for the ease of computation can produce visually interesting simulations with unphysical dynamics.

Our goal is to develop a numerical scheme that is accurate and efficient in computing a Navier-Stokes flow around moving particles while taking into account the effect of the lubrication forces on the collisions. The method presented here include two essential parts. First, to simulate interactions between freely moving particles and the surrounding flow, we solve the Navier-Stokes equations coupled to the particle dynamics using the immersed interface method. An advantage of the immersed interface method is its use of a fixed Cartesian grid, which saves the cost of grid regeneration. In order to resolve the sharp moving interfaces and the coupled dynamics, we have developed an algorithm that has improved the accuracy and the efficiency of existing methods [9,8,10–13,1,14]. The main challenge for the current work is to correctly account for the physics of particle collisions. We note that the fluid in the thin gap between the particles during collision is governed by the lubrication theory, while the bulk flow is governed by the Navier-Stokes equations. Therefore, in principle we can integrate the lubrication solutions with the immersed interface method to capture the lubrication forces during particle collisions. The use of lubrication solution in the gap would eliminate the need for local grid-refinement. The key is to derive a method that has a two-way coupling between the Navier-Stokes solutions and the lubrication solutions. In addition, both flows should be coupled directly to the dynamics of the moving particles.

In the following sections, we provide an algorithm for the treatment of these different kinds of couplings. In order to test our method and to understand the basic mechanisms during collisions, we choose to study four fundamental collision processes so that the numerical results can be compared against the analytic solutions. The method is not limited to these testing cases, and can be applied to collisions between two surfaces of arbitrary shapes moving in any relative motion. For this, we provide the lubrication solutions in the more general cases, so that the algorithms can be readily extended.

2. Method

The main building blocks for the method include the immersed interface method, which computes the coupling between the particles and the flow, the lubrication theory, which computes the flow in the gap between particles, and the integration of the Navier-Stokes solutions and the lubrication solutions in order to handle particle collisions.

2.1. The immersed interface method

To compute freely moving particles in a Navier-Stokes flow, we have developed an algorithm in the framework of immersed interface methods [4,5,9,8,10–14,1]. The immersed interface method provides a general framework for solving PDEs involving interfaces. Similar to the immersed boundary method [6], it implements the boundary conditions at the moving interface between the solid and the fluid by introducing a singular force distribution along the interface in the Navier-Stokes equations. The accuracy of the solutions depends on how to numerically handle this singular force distribution. In the immersed boundary method, the delta function associated with the singular force is directly approximated. In the immersed interface method, the delta function is integrated to derive jump conditions for discontinuities in piecewise smooth solutions, and the jump conditions are incorporated into the numerical schemes. It is possible to derive all the necessary jump conditions for velocity and pressure derivatives from the Navier-Stokes equations [9]. The flow can be solved using a finite difference scheme that takes into account the proper jump conditions [8]. The solution gives the desired flow exterior to the particles.

To study particle-flow interactions, it is essential to solve the particle dynamics simultaneously. In order to model the rigid body dynamics of the particle, we introduce a body force that guarantees the interior fluid to behave as a rigid body [11,13]. The body force can be viewed as an external force field acting on a piece of fluid such that the fluid translates and rotates in a rigid motion. The body force corresponding to rotation behaves like pressure, and the body force corresponding to angular acceleration acts as an external force. When the body force is included in the Navier-Stokes equation along with the singular force distribution, the solution then gives the correct coupled dynamics between the moving particles and the flow.

The nondimensional Navier-Stokes equations governing the flow coupled to freely moving rigid body are given by,

$$\frac{\partial \vec{v}}{\partial t} + \vec{v}\cdot\nabla\vec{v} = -\nabla p + \frac{1}{Re}\nabla^2\vec{v} + \int_\Gamma \vec{f}(\alpha,t)\delta(\vec{x}-\vec{X}(\alpha,t))\,d\alpha \;+\vec{b}, \tag{1a}$$

$$\nabla\cdot\vec{v} = 0, \tag{1b}$$

where $\vec{v}=(u,v)$ and p are the fluid velocity and pressure, Re is the Reynolds number, $\vec{f}$ is the singular force density along the interface and $\vec{b}$ is the body force on the object due to angular acceleration. In the Dirac delta function $\delta(\vec{x}-\vec{X}(\alpha,t))$, $\vec{x}$ is a point in the computational domain, $\vec{X}(\alpha,t)$ is a point on the interface Γ, and $\alpha\in[0,2\pi)$ is a nondimensional parameter parametrizing Γ with the Jacobian $J=||\partial\vec{X}/\partial\alpha||_2$ (Fig. 1). By convention, Equations (1a), (1b) are nondimensionalized using the fluid density $\rho_{\mathbf{f}}$, the characteristic length $\mathbf{l}$, and the characteristic velocity $\mathbf{u}$ of the flow. The Reynolds number $Re=\rho_{\mathbf{f}}\mathbf{ul}/\nu$, where ν is the kinematic viscosity of the fluid. All variables in subsequent discussions will be nondimensionalized in the same way. Dimensional quantities will be denoted using a bold font.

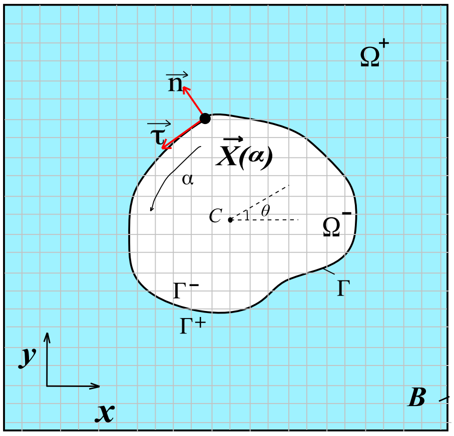

Fig. 1. Geometries for flow around an immersed object (reproduced from [1]).

The singular force needed to enforce the no-slip and no-penetration boundary conditions on Γ can be derived from the Navier-Stokes equations [11–13]. The tangential and normal components of the force density are given by,

$$f_\tau \equiv \frac{\vec{f}\cdot\vec{\tau}}{J} = -\frac{1}{Re}(\omega^+ - \omega^-) = -\frac{1}{Re}\left(\vec{\tau}\cdot\frac{\partial \vec{v}}{\partial n}\bigg|^+ - \frac{d\theta}{dt}\right), \tag{2a}$$

$$f_n \equiv \frac{\vec{f}\cdot\vec{n}}{J} = \int \frac{\partial f_n}{\partial \alpha}d\alpha, \quad \frac{\partial f_n}{\partial \alpha} = J\left(\frac{1}{Re}\,\frac{\partial \omega}{\partial n}\bigg|^+ + [\vec{b}]\cdot\vec{\tau}\right), \tag{2b}$$

where $\omega = \partial v/\partial x - \partial u/\partial y$ is the vorticity, $\vec{\tau} = (1/J)(\partial\vec{X}/\partial\alpha)$ the unit tangent vector to Γ, $\partial/\partial n$ the normal derivative on Γ (see Fig. 1), and $[b] = b|_{\Gamma^+} - b|_{\Gamma^-}$ the jump condition for the discontinuity in b across Γ.

In order to find the body force $\vec{b}$ acting on the particle, we note that the rigid body motion of the fluid enclosed by the boundary Γ can be expressed as a solution to [11,13],

$$\frac{d\vec{v}}{dt} = -\nabla p + \frac{1}{Re}\nabla^2\vec{v} + \vec{b}.$$

In 2D,

$$p = -\frac{d^2x_c}{dt^2}x - \frac{d^2y_c}{dt^2}y + \frac{1}{2}\left(\frac{d\theta}{dt}\right)^2[(x-x_c)^2 + (y-y_c)^2],$$

and the body force $\vec{b} = (b_x, b_y)$ that depends on the angular acceleration is given as

$$b_x = -\frac{d^2\theta}{dt^2}(y - y_c), \tag{3a}$$

$$b_y = \frac{d^2\theta}{dt^2}(x - x_c), \tag{3b}$$

where $\vec{x}_c(t) = (x_c, y_c)$ and $\theta(t)$ are the center of mass position and the orientation of the particle, respectively (Fig. 1). Since the body force $\vec{b}$ is only nonzero inside the particle, it is discontinuous across Γ.

2.2. Particle dynamics

The equations of the motion for the moving particle are given by

$$m_s\frac{d\vec{v}_c}{dt} = \vec{F}_e + \vec{F}_f, \tag{4a}$$

$$I\frac{d^2\theta}{dt^2} = T_e + T_f, \tag{4b}$$

where m_s is the nondimensional mass of the object, $\vec{v}_c$ is the velocity of the center of mass in the lab frame, I is the moment of inertia with respect to the center of mass, $\vec{F}_e$ is the external non-fluid force on the object (e.g. buoyancy corrected weight), $\vec{F}_f$ is the fluid force on the object, T_e is the external torque on the object with respect to the center of

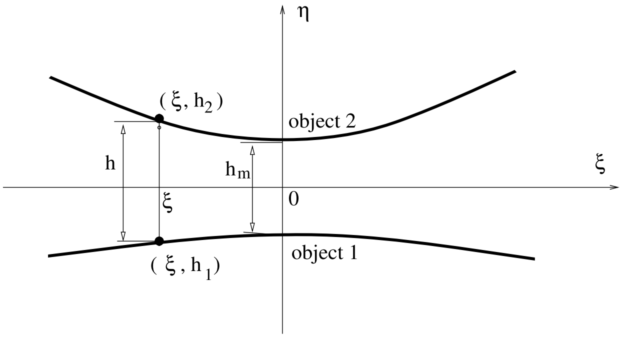

Fig. 2. Sketch of two objects in close contact. At abscissa ξ, the separation between the two object surfaces is $h = h_2 - h_1$. h_m is the minimum separation at $\xi = 0$.

mass, and T_f is the fluid torque on the object with respect to the center of mass. The fluid force and torque acting on the object can be expressed as

$$\vec{F}_f = -\int_{\Gamma} \left(f_\tau \vec{\tau} + p^+ \vec{n} \right) J\mathrm{d}\alpha, \tag{5a}$$

$$\vec{T}_f = -\int_{\Gamma} (\vec{X} - \vec{x}_c) \times \left(f_\tau \vec{\tau} + p^+ \vec{n} \right) J\mathrm{d}\alpha. \tag{5b}$$

Together, equations (1)–(5) govern the dynamic coupling between the particle and the Navier-Stokes flow. The algorithm for solving this set of equations are described in [8,1].

2.3. Lubrication solutions in the gap between two particles

The main idea for the current work is to compute the collision dynamics by integrating the Navier-Stokes solutions in the bulk flow and the lubrication solutions in the interstitial flow between particles that are in close proximity. The use of lubrication solutions for the flow in the gap eliminate the restriction on the grid resolution in the gap. For the method to work, first we need to find expressions for the lubrication solutions in general cases where two particles interact.

Consider the generic case of two surfaces of arbitrary shapes moving in a relative motion in a fluid (Fig. 2). The flow in the gap is governed by the lubrication equations:

$$\frac{\partial \hat{u}}{\partial \xi} + \frac{\partial \hat{v}}{\partial \eta} = 0, \tag{6a}$$

$$\frac{\partial^2 \hat{u}}{\partial \eta^2} = Re \frac{dp}{d\xi}, \quad p = p(\xi), \tag{6b}$$

where $\hat{u}$ and $\hat{v}$ are the velocity components along the ξ and η axes in Fig. 2, respectively. The lubrication equations holds when $h \ll 1$ and $Re\, h^2 \ll 1$, where $h = h(\xi, t)$ is the non-dimensional gap height (non-dimensionalized by the same characteristic length **l** used to define the Reynolds number Re).

Given the geometries and motions of the two surfaces, the flow in the lubrication gap can be found by solving equations (6a) and (6b) subject to the no-slip and no-penetration boundary conditions. Integrating equation (6b) twice gives,

$$\hat{u} = \hat{u}_1 + \frac{\hat{u}_2 - \hat{u}_1}{h}(\eta - h_1) + \frac{Re}{2}\frac{dp}{d\xi}\left((\eta - h_1)^2 - (\eta - h_1)h \right), \tag{7}$$

where $\hat{u}_1(\xi, t)$ is the ξ-component of the velocity of a point on the object 1, and $\hat{u}_2(\xi, t)$ on the object 2. Substituting equation (7) in equation (6a) and then integrating with respect to η from h_1 to h_2 leads to the Reynolds equation [7]

$$\frac{\partial h}{\partial t} + \frac{\partial}{\partial \xi}\left(\frac{\hat{u}_1 + \hat{u}_2}{2} h \right) + \hat{u}_1 \frac{\partial h_1}{\partial \xi} - \hat{u}_2 \frac{\partial h_2}{\partial \xi} = \frac{Re}{12}\frac{\partial}{\partial \xi}\left(h^3 \frac{dp}{d\xi} \right). \tag{8}$$

Further integrating equation (8) gives the pressure derivative needed in equation (7),

$$\frac{dp}{d\xi} = \frac{12}{Reh^3}\left(\frac{\partial h}{\partial t}\xi + \frac{\hat{u}_1 + \hat{u}_2}{2} h + \int_{\xi_0}^{\xi} \left(\hat{u}_1 \frac{\partial h_1}{\partial \xi} - \hat{u}_2 \frac{\partial h_2}{\partial \xi} \right) d\xi + C \right), \tag{9}$$

where the integration constant C can be found by evaluating equation (9) at a specific $\xi = \xi_0$,

$$C = \frac{Reh(\xi_0,t)^3}{12}\left.\frac{dp}{d\xi}\right|_{\xi=\xi_0} - \xi_0\left.\frac{\partial h}{\partial t}\right|_{\xi=\xi_0} - \frac{\hat{u}_1(\xi_0,t)+\hat{u}_2(\xi_0,t)}{2}h(\xi_0,t). \tag{10}$$

In general, we can choose either $\xi_0 = \xi_L$ or $\xi_0 = \xi_R$ as shown in Fig. 4 that separates the inside and outside of the lubrication region. At $\xi_0 = \xi_L$ (or $\xi_0 = \xi_R$), we can compute f_τ using both the finite difference scheme for Equation (2a) and the analytical expression in Equation (13). Matching the two computed values determines the value of $dp/d\xi|_{\xi=\xi_0}$. In special cases, $dp/d\xi|_{\xi=\xi_0}$ can also be determined by symmetry.

2.4. Coupling the Navier-Stokes solutions and the lubrication solutions

The integration between the immersed interface method and the lubrication solution is done in the singular force calculations. To evaluate the singular force distribution on a surface next to the lubrication layer, we make use of the lubrication solutions to calculate ω and $\frac{\partial\omega}{\partial n}$:

$$\omega = \frac{\partial \hat{v}}{\partial \xi} - \frac{\partial \hat{u}}{\partial \eta} \approx -\frac{\partial \hat{u}}{\partial \eta}, \tag{11a}$$

$$\frac{\partial \omega}{\partial n} = \frac{\partial \omega}{\partial \xi}n_\xi + \frac{\partial \omega}{\partial \eta}n_\eta \approx -\frac{\partial^2 \hat{u}}{\partial \eta^2}n_\eta = -Re\frac{dp}{d\xi}n_\eta, \tag{11b}$$

where n_ξ and n_η are the ξ and η components of the outward unit normal vector $\vec{n}$ to the surface, respectively. Note that we have applied Equation (6b) in Equation (11b).

Substituting these into equations (2a), (11a) and using the fact that $\omega^- = 2d\theta/dt$ give the tangential component of the singular force density on the lubrication portion of the surface,

$$f_\tau \approx \frac{1}{Re}\left(\left.\frac{\partial \hat{u}}{\partial \eta}\right|^+ + 2\frac{d\theta}{dt}\right). \tag{12}$$

Evaluating $\partial\hat{u}/\partial\eta|^+$ in equation (12) at the object 1 and 2 in Fig. 2, i.e. at $\eta = h_1$ and $\eta = h_2$, and using equation (7) for $\hat{u}$, we obtain f_τ for the two objects,

$$f_{\tau 1} \approx \frac{1}{Re}\left(\frac{\hat{u}_2 - \hat{u}_1}{h} - \frac{Re}{2}\frac{dp}{d\xi}h + 2\frac{d\theta_1}{dt}\right), \tag{13a}$$

$$f_{\tau 2} \approx \frac{1}{Re}\left(\frac{\hat{u}_2 - \hat{u}_1}{h} + \frac{Re}{2}\frac{dp}{d\xi}h + 2\frac{d\theta_2}{dt}\right), \tag{13b}$$

where $dp/d\xi$ is given by equation (9).

Likewise, equations (2b), (11b) gives the normal component of the singular force density on the lubrication portion of each surface,

$$f_n \approx \int J\left(-\frac{dp}{d\xi}n_\eta + [\vec{b}]\cdot\vec{\tau}\right)d\alpha\,. \tag{14}$$

2.5. Numerical implementation

Fig. 3 outlines the key steps for integrating the lubrication solutions with the Navier-Stokes solutions. The lubrication approximations are triggered when the minimal gap size between the two surfaces is less than a critical distance. In the general system of n particles with different shapes, we need to identify the distances between pair-wise particles, which is a geometry problem. One way to do this efficiently is to assign an integer value to each grid point: zero for the fluid, k for the interior points of the kth object, $k = 1, 2, \cdots, n$. To determine whether a marker point belongs to the lubrication region, we can draw a normal line of a critical length from the marker point. If the line ends in a grid cell that has at least one interior grid point, then the lubrication approximations are used for evaluating singular forces at the marker. Along each surface, we identify the region where the lubrication solutions are needed and then apply the lubrication solutions to evaluate f_τ and f_n (Section 2.4). Outside the lubrication region, we still use finite differences for equations (2a) and (2b) directly. In the case of collision between two objects, it is straightforward to calculate the minimal distance between them.

Our immersed interface method employs the MAC scheme with explicit time stepping [8]. Before the collision, the time step δt of a simulation is given by the CFL conditions,

$$\delta t = 0.5\min\left[\left(\frac{u_{\max}}{\delta x} + \frac{v_{\max}}{\delta y}\right)^{-1}, Re\left(\frac{1}{\delta x^2} + \frac{1}{\delta y^2}\right)^{-1}\right], \tag{15}$$

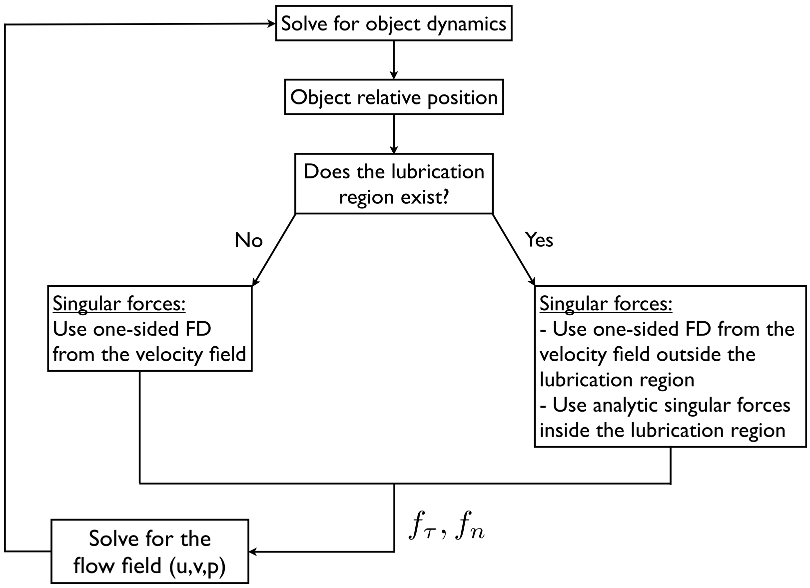

Fig. 3. The flow chart of the coupling between the Navier-Stokes solutions and the lubrication solutions.

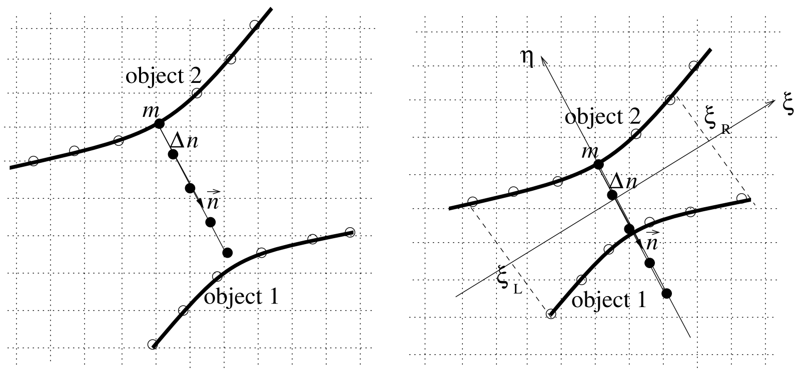

(a) *Before collision* (b) *After collision*

Fig. 4. Sketch of two approaching objects in a Cartesian grid before (left) and after (right) the onset of lubrication approximations. The lubrication approximations are triggered when the normal distance from one object surface to the other is less than $4\Delta n$. The lubrication region corresponds to $\xi_L \le \xi \le \xi_R$. The open circles are Lagrange markers indexed with m to represent the object surfaces.

where $u_{\max}$ and $v_{\max}$ are the maximum u and v in the current flow field, respectively. After a collision is triggered, we need to choose a time scale to capture the collision dynamics. The relevant time scale for a collision can be estimated by momentum balance, $F\delta t \sim m_s \delta v$, where m_s is the mass of an object, δv is the change of its speed, and F is the pressure force acting on the object. We estimate F by equation (9), $F \sim (12\partial h_m/\partial t)/(Reh_m^3)$. We have the estimation $m_s\delta v \sim \gamma \partial h_m/\partial t$. This gives a choice for the new time step,

$$\delta t = \frac{\gamma Reh_m^3}{12}. \tag{16}$$

3. Results

The method described above applies to general cases of collisions between particles of arbitrary shapes moving in relative motions. Our current goal for the simulations is to find examples where we can test the method against analytic solutions. For this, we restrict ourselves to four fundamental cases: (1) the vertical fall of a cylinder toward a fixed wall, (2) a fixed cylinder over a translating wall, (3) a rotating cylinder over a fixed wall, and (4) the collision between two identical cylinders. The first and second are studies of normal and tangential collisions of a translating particle, the third is a study of the collision of a rotating particle, and in the last case, we also examine the effects of the Reynolds number and the grid resolution.

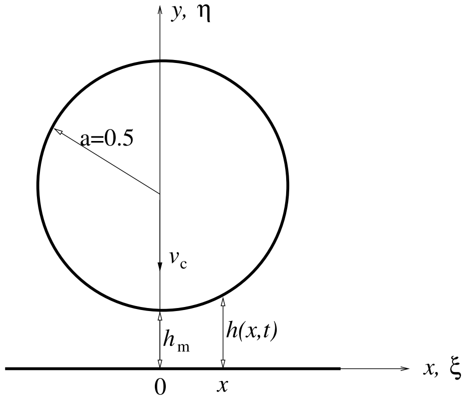

Fig. 5. Sketch of a cylinder of radius a falling vertically toward a fixed wall with the velocity v_c. h is the height of the point P, and h_m is the minimum gap height.

3.1. Parameters in the simulation

The computations are carried out in dimensionless forms. In all the cases, we have a natural length scale, the diameter of a cylinder, **l**, so the non-dimensional radius of the cylinder is $a = 0.5$. The velocity scale, **u** is chosen according to the flow characteristics in each case. The computational domain is a rectangle. Neumann boundary conditions for the pressure are applied on the four sides of the computational domain, and homogeneous Neumann boundary conditions for the velocity are applied on a side that is not a solid wall. In all the cases, the density ratio of a cylinder to the fluid is fixed to be $\gamma = 1.5$, and the cylinder is parametrized by 512 equally spaced Lagrangian points fixed on its surface.

3.2. Vertical fall of a cylinder toward a fixed wall

To study the normal collision, we consider the free fall of a cylinder in a fluid under gravity toward a fixed wall (Fig. 5). The velocity scale **u** is chosen as the terminal velocity of the cylinder assuming a drag coefficient of unity, $\mathbf{u} = \sqrt{(\gamma - 1)\pi \mathbf{g}\mathbf{l}/2}$. The Reynolds number is $Re = 10$.

The size of the rectangular computational domain is 4×8, and the grid resolution is $\delta x \times \delta y = (1/80) \times (1/160)$. The lubrication approximations are triggered when the distance along the normal direction of the cylinder from a marker point to a point on the bottom wall is less than $h_0 = 4\sqrt{\delta x^2 + (2\delta y)^2} \approx 0.07$. At the onset of the lubrication approximations, there are about 11 grid points along the vertical direction in the gap with this choice of h_0 (instead of $h_0 = 4\Delta n \approx 4\sqrt{\delta x^2 + \delta y^2}$), which allows us to resolve the flow in the gap using the Navier-Stokes solver and the new method, so that we can compare the two results.

To evaluate f_τ and f_n, we note that the lubrication equations (7) and (9) in this case become

$$u = \frac{Re}{2}\frac{dp}{dx}y(y-h), \tag{17a}$$

$$\frac{dp}{dx} = \frac{12}{Re}\frac{x}{h^3}\frac{\partial h}{\partial t}. \tag{17b}$$

Note that $dp/dx = 0$ at $x = 0$, due to symmetry. Following Equations (13a) and (14), we have

$$f_\tau \approx \frac{h}{2}\frac{dp}{dx}\,, \tag{18}$$

$$f_n \approx -\int n_y \frac{dp}{dx} J d\alpha\,, \tag{19}$$

where $n_y = -\sqrt{1-(x/a)^2}$. Since the body does not rotate, $\vec{b} = 0$. The lubrication approximations enter the Navier-Stokes solver only through the computation of the singular force. The velocity and the pressure at the grid points in the gap are computed together with the rest of the flow in the Navier-Stokes solver, thus we have a smooth velocity and pressure fields across the two regions.

Fig. 6 shows the full time series of the acceleration, velocity, and minimum gap size for the cylinder. The cylinder accelerates towards the wall from the rest with a decreasing acceleration due to the drag, and then decelerates almost to a stop rather abruptly as it gets close to the wall.

It is worth noting that in this case the lubrication force is sufficient to prevent direct contact between the cylinder and the wall, independent of the weight and the initial velocities of the cylinder, and the gap size approaches zero asymptotically, as shown in reference [2]. In other words, there is no rebound during such a collision. Had we used an dry collision

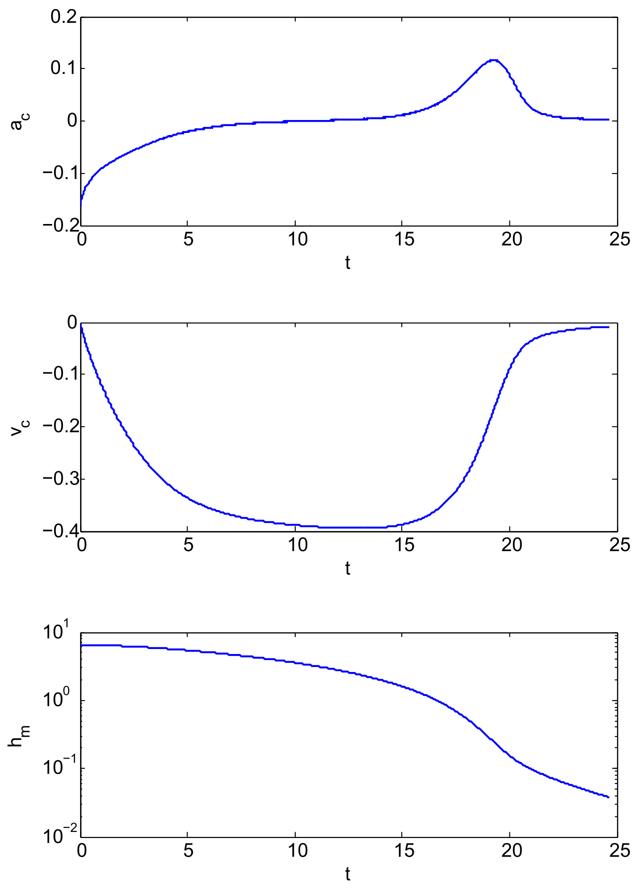

Fig. 6. Acceleration, velocity and gap height of a cylinder falling vertically toward a fixed wall.

rule, e.g., the elastic collision between two particles, it would automatically produces a rebound, because the incoming velocity toward the wall is non-zero, and by the conservation of momentum and energy, the rebound velocity would be non-zero, too.

One way to check the code is to compare the flow computed using the new method to the flow computed using the original Navier-Stokes solver in the regime where the gap is small enough for the lubrication approximation to hold and large enough for the finite difference approximations also to work when compute f_τ and f_n. The comparisons are shown in Fig. 7. After the lubrication approximations are triggered, the Navier-Stokes solutions agrees very well with the lubrication solutions from Equations (17a) and (17b) even though the lubrication approximations enters the Navier-Stokes solver only through the computation of the singular force. The corresponding singular forces are shown in Fig. 8.

3.3. Fixed cylinder above a translating wall

Next we consider a tangential collision between a cylinder and a wall in which the shear forces are important. In this case, the velocity scale is chosen as the translating speed of the wall, so the tangential velocity of the wall is $\vec{v} = (U, 0) = (1, 0)$. The cylinder is held static. The Reynolds number is $Re = 10$. The size of the computational domain is 16×4, and the grid resolution is $\delta x \times \delta y = (1/80) \times (1/160)$. The gap distance between the cylinder and the wall is fixed at $h_m = 0.05$, a height at which the lubrication approximations are valid.

With the boundary conditions $u_1 = U$, $u_2 = 0$, the lubrication solutions are given by

$$u = U\left(1 - \frac{y}{h}\right) + \frac{Re}{2}\frac{dp}{dx} y(y-h)\,. \tag{20}$$

To find the pressure derivative dp/dx, we note that the only non-zero term on the left-hand side of Equation (8) is

$$\frac{\partial}{\partial x}\left(\frac{u_1 + u_2}{2} h\right) = \frac{U}{2}\frac{dh}{dx}\,,$$

and Equation (9) becomes

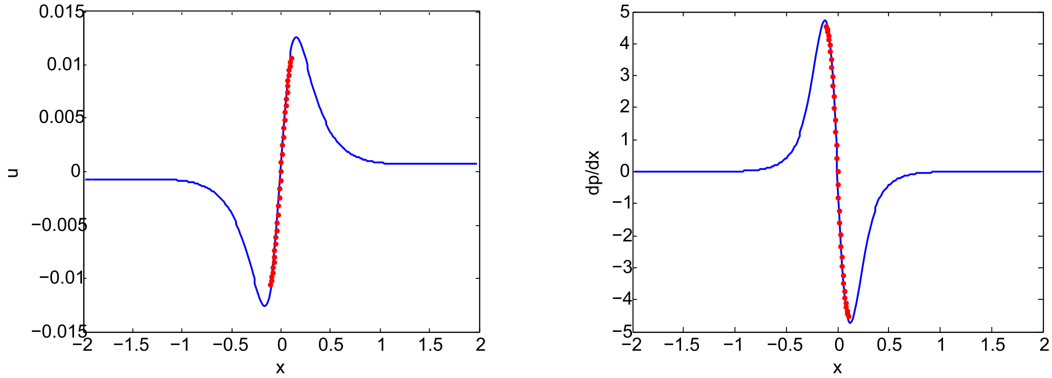

Fig. 7. Comparisons between the Navier-Stokes solutions (blue, solid line) and analytical solutions (red, dots) for the fluid velocity u and the pressure derivative dp/dx in a flow due to a cylinder falling vertically toward a fixed wall. The data are computed at the grid line of $y \approx 0.009368$ parallel and near the bottom wall at the time $t = 22.0932$ shortly after the lubrication approximations are triggered at $t = 22.0900$. (For interpretation of the colors in the figure(s), the reader is referred to the web version of this article.)

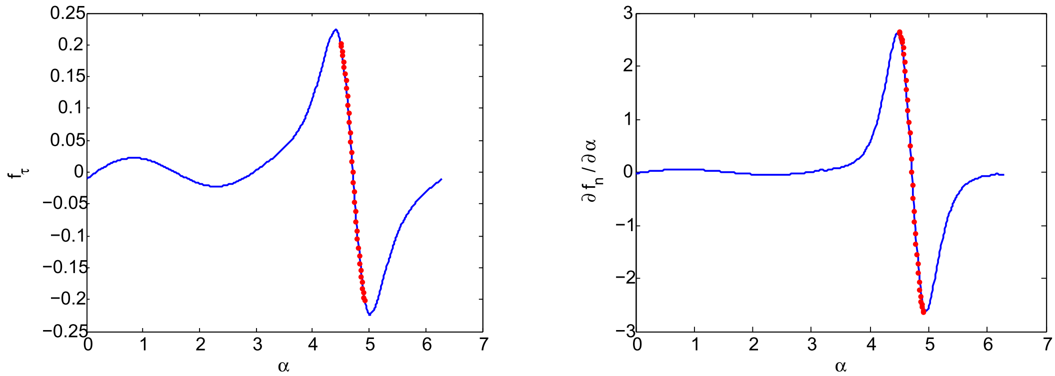

Fig. 8. Comparisons of the singular force distributions at the time $t = 22.0932$ shortly after the lubrication approximations are triggered at $t = 22.0900$ in a flow due to a cylinder falling vertically toward a fixed wall. Solid lines: numerical data from one-sided finite differences. Dots: analytical data from Equations (18) and (19).

$$\frac{dp}{dx} = \frac{12}{Reh^3}\left(\frac{U}{2}h + C\right), \tag{21}$$

where C is the integration constant, which can be determined from

$$\left.\frac{dp}{dx}\right|_{x=0} = \frac{12}{Reh_m^3}\left(\frac{U}{2}h_m + C\right), \tag{22}$$

where $(dp/dx)_{x=0}$ can be approximated, at each time step, from the current numerical pressure field, using a centered finite-difference scheme along the bottom wall at $x = 0$ as

$$\left.\frac{dp}{dx}\right|_{x=0} \approx \frac{p(\Delta x) - p(-\Delta x)}{2\Delta x}. \tag{23}$$

Combining Equations (21) and (22), we obtain the solution for the pressure derivative dp/dx in the lubrication limit:

$$\frac{dp}{dx} = \frac{6U}{Re\,h^2}\left(1 - \frac{h_m}{h}\right) + \left(\frac{h_m}{h}\right)^3 \left.\frac{dp}{dx}\right|_{x=0}. \tag{24}$$

The tangential and normal components of the singular force in Equation (13) for the cylinder are given by

$$f_\tau \approx -\frac{U}{Re\,h} + \frac{h}{2}\frac{dp}{dx}\,. \tag{25}$$

$$f_n \approx -\int n_y \frac{dp}{dx} J d\alpha\,. \tag{26}$$

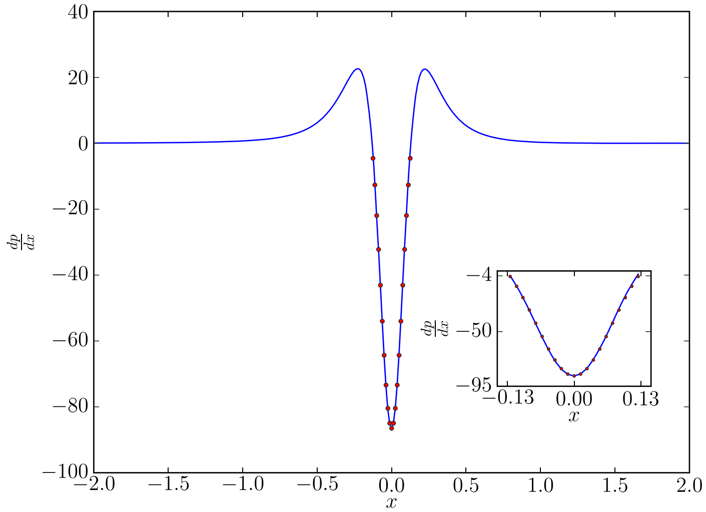

Fig. 9. Steady pressure derivative dp/dx on the bottom-most grid line for a cylinder fixed over a translating wall. Numerical (solid, blue) and analytical (Equation (24)) (dots, red) data. The inset zooms on the lubrication region.

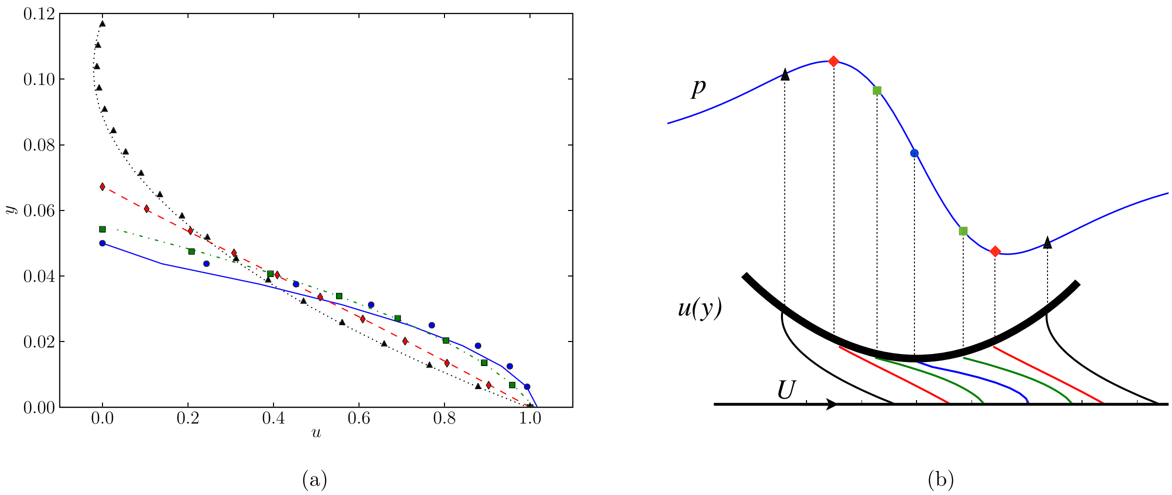

Fig. 10. Velocity profile $u(y)$ at different x locations in the gap between a fixed cylinder and a wall translating at the velocity $U = 1$. (a) Numerical (curves) and analytic (symbols) data: at the middle ($x = 0$, blue, solid, circles), half-way ($x = x_L/2 = 0.065$, green, dot-dashed, squares), exit ($x = x_L = 0.13$, red, dashed, diamonds), and outside ($x = a/2 = 0.25$, black, dotted, triangles) of the lubrication region. (b) Pressure and velocity profiles at the corresponding and symmetric points in (a). The thick arc represents the cylinder.

Fig. 9 shows the pressure derivative dp/dx along the bottom-most grid line of the domain. The comparison between the Navier-Stokes and analytic solutions in the lubrication region shows good agreement.

Fig. 10(a) shows the velocity profiles across the gap at four different locations: the middle ($x = 0$), half-way ($x = x_L/2 = 0.065$), exit ($x = x_L = 0.13$) and outside ($x = 0.25$) of the lubrication region, where the abscissa x_L is the x-coordinate of the rightmost marker point on the cylinder in the lubrication region. The velocity profile $u(y)$ at a given x location is composed of a linear part and a quadratic part. The shape of the velocity profile depends on the relative magnitudes of these two contributions, and the concavity of the profile is determined by the sign of the pressure derivative dp/dx (Fig. 9). The numerical data from the Navier-Stokes solver agree well with the analytic solutions.

The pressure profile in Fig. 10(b) creates a clockwise torque on the cylinder about its center of mass, which is to separate the cylinder from the wall on the left and attract on the right. In contrast, the shear force on the cylinder in the lubrication region creates a counterclockwise torque. The torque due to this shear force in the lubrication region is

$$T_\mu^L = -a \int\limits_{\Gamma_L} f_\tau \, d\theta \tag{27}$$

where f_τ is given by Equation (25), θ is the central angle of the cylinder measured counterclockwise, and Γ_L denotes the lubrication part on the cylinder. Note that the cylinder is kept static even though it experiences the fluid force and torque. Below we give an analytical estimate of the torque due to the shear force for a lubrication region of small $|\theta|$. With Equations (24) and (25), Equation (27) can be written as

$$T^L_\mu = -\frac{2Ua}{Re}\underbrace{\int_{\Gamma_L}\frac{d\theta}{h}}_{(1)} + a\left(\frac{3Uh_m}{Re} - \frac{h_m^3}{2}\left.\frac{dp}{dx}\right|_{x=0}\right)\underbrace{\int_{\Gamma_L}\frac{d\theta}{h^2}}_{(2)} \tag{28a}$$

where $h = h_m + a(1-\cos\theta) \approx h_m + a\theta^2/2$ for small $|\theta|$ and

$$(1) \approx \frac{2\pi}{a}\left(\frac{a}{2h_m}\right)^{1/2}, \qquad (2) \approx \frac{2\pi}{a^2}\left(\frac{a}{2h_m}\right)^{3/2}.$$

So we have

$$T^L_\mu \approx -\frac{\pi U}{Re}\left(\frac{a}{2h_m}\right)^{1/2} - \frac{\sqrt{2}\pi}{4}\left.\frac{dp}{dx}\right|_{x=0}(h_m^3 a)^{1/2}. \tag{28b}$$

The leading term of $\mathcal{O}((a/h_m)^{1/2})$ is

$$T^L_\mu \approx -\frac{\pi U}{Re}\left(\frac{a}{2h_m}\right)^{1/2}. \tag{28c}$$

3.4. Rotating cylinder over a fixed wall

So far we have considered the translational motion. In this example, we study a rotating cylinder over a fixed wall. In this case, the velocity scale is chosen such that the non-dimensional angular velocity of the cylinder is $d\theta/dt = 1$. The Reynolds number is $Re = 10$. The size of the rectangular computational domain is 16×4, and the grid resolution is $\delta x \times \delta y = (1/80) \times (1/160)$. The gap distance is kept fixed with $h_m = 0.05$.

In this case, the boundary conditions are give by $u_1 = 0$ and $u_2 = \dot{\theta}\sqrt{a^2 - x^2}$, the solutions to the lubrication equation (7) are

$$u = \frac{\dot{\theta}\sqrt{a^2-x^2}}{h}y + \frac{Re}{2}\frac{dp}{dx}y(y-h). \tag{29}$$

To find dp/dx, we note that the volume flow rate Q across the gap is

$$Q = \int_0^h u\,dy = \frac{\dot{\theta}\sqrt{a^2-x^2}h}{2} - \frac{Re\,h^3}{12}\frac{dp}{dx}, \tag{30}$$

which gives

$$\frac{dp}{dx} = \frac{6\dot{\theta}\sqrt{a^2-x^2}}{Re\,h^2} - \frac{12Q}{Re\,h^3}. \tag{31}$$

According to Equation (6a), the flow rate Q satisfies

$$\frac{dQ}{dx} = -\int_0^h \frac{\partial v}{\partial y}dy = -v(x,h) = -\dot{\theta}x \tag{32}$$

$$\Rightarrow \qquad Q(x) = -\frac{\dot{\theta}x^2}{2} + Q(0), \tag{33}$$

where $Q(0)$ is given by Equation (30) as

$$Q(0) = \frac{\dot{\theta}ah_m}{2} - \frac{Re\,h_m^3}{12}\left.\frac{dp}{dx}\right|_{x=0}, \tag{34}$$

with $(dp/dx)_{x=0}$ approximated by Equation (23). Substituting the expression of Q given by Equation (33) into Equation (31), we obtain dp/dx.

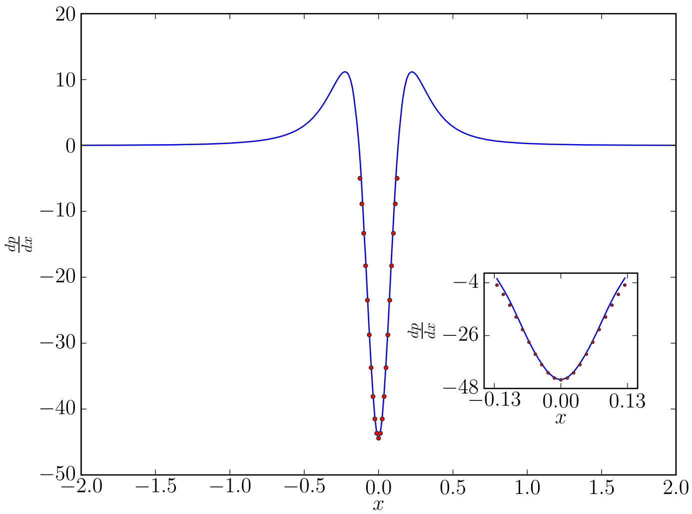

Fig. 11. Steady pressure derivative dp/dx on the bottom-most grid line for a cylinder rotating above a fixed wall. Numerical (solid, blue) and analytical (Equation 31) (dots, red) data. The inset zooms on the lubrication region.

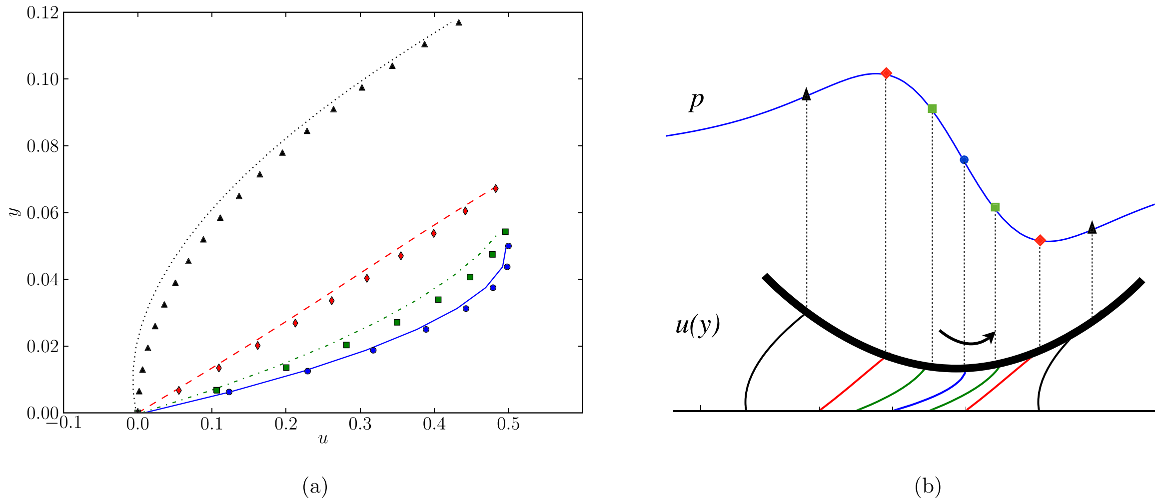

Fig. 12. Velocity profile $u(y)$ in the gap between a cylinder rotating above a fixed wall at different x locations. (a) Numerical (curves) and analytic (symbols) data: at the middle ($x = 0$, blue, solid, circles), half-way ($x = x_L/2 = 0.065$, green, dot-dashed, squares), exit ($x = x_L = 0.13$, red, dashed, diamonds), and outside ($x = a/2 = 0.25$, black, dotted, triangles) of the lubrication region. (b) Pressure and velocity profiles at the corresponding and symmetric points in (a). The thick arc represents the rotating cylinder.

The tangential and normal components of the singular force in Equation (13) on the cylinder are

$$f_\tau \approx \frac{\dot{\theta}}{Re}\left(\frac{\sqrt{a^2 - x^2}}{h} + 2\right) + \frac{h}{2}\frac{dp}{dx}\,. \tag{35}$$

$$f_n \approx -\int n_y \frac{dp}{dx} J d\alpha\,. \tag{36}$$

where dp/dx is given by Equation (31).

Again in this case, we find good agreement between the Navier-Stokes solutions and the lubrication solutions (Fig. 11, Fig. 12). In this case flow is separated, as seen in the vorticity contours in Fig. 13. The locations of the separation points and the reattachment points on the wall are determined by

$$\left.\frac{\partial u}{\partial y}\right|_{y=0} = 0. \tag{37}$$

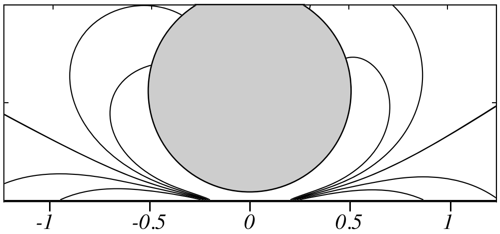

Fig. 13. Vorticity contours for a cylinder rotating above a fixed wall.

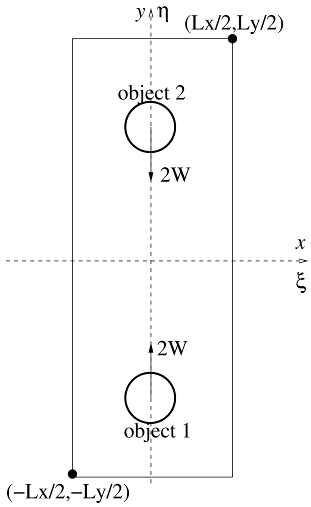

Fig. 14. Two identical cylinders approaching each other in a rectangular domain, each driven by a constant force $2W$.

This provides another check for the code. The lubrication solution to Equation (37) has four roots, two positive and two negative. Of the positive ones, one is a separation point, x_{SP}, and the other is a reattachment point, x_{RP}, with $x_{SP} < x_{RP}$. For $x_{SP} > 0$, we find $x_{SP} \approx 0.254$. Numerically, it is sufficient to find the positive x-coordinate of the point on the wall where the vorticity is zero since $\omega = \partial v/\partial x - \partial u/\partial y = -\partial u/\partial y$ on the wall, which gives $x_{SP} \approx 0.212$. We note that the numerical value is close to the value $x_{SP} \approx 0.223$ (measured in our unit), reported in [3].

3.5. Head-on collisions between two cylinders

In the final example, we simulate the head-on collision of two identical cylinders in a fluid at $Re = 10$ and $Re = 100$ (Fig. 14). In the case of $Re = 10$, we also compare the results using two grid resolutions. These cases further show that the simulation works when the gap height is well below the grid resolution in both cases.

In these cases, the cylinders are pulled toward each other along the center line, by a constant force twice the weight of the cylinder, $F = 2W = \gamma/(\gamma - 1)$, and there is no additional gravity. The singular force densities on the cylinders are

$$f_{\tau 1} \approx -\frac{h}{2}\frac{dp}{dx}, \quad f_{\tau 2} \approx \frac{h}{2}\frac{dp}{dx}, \quad f_n \approx -\int n_y \frac{dp}{dx} J d\alpha \ , \tag{38}$$

where $n_y = \sqrt{1-(x/a)^2}$ and $-\sqrt{1-(x/a)^2}$ for the cylinders 1 and 2, respectively, with the pressure gradient given by,

$$\frac{dp}{dx} = \frac{12}{Re}\frac{x}{h^3}\frac{\partial h}{\partial t} \ . \tag{39}$$

Fig. 15 shows the time series of h_m and v_c at $Re = 10$, and $Re = 100$. In both cases, the minimum gap reaches a distance well below the grid resolution. The lubrication approximations are triggered when the minimal distance between the cylinders is less than $h_0 \approx 4\sqrt{\delta x^2 + \delta y^2}$. At $Re = 10$, the minimum gap height reaches $h_m \approx 0.0048$, which is well below the resolutions, $\delta x = \delta y = 0.0125$ in one case, and $\delta x = \delta y = 0.025$ in the other. At $Re = 100$, the minimum gap height reaches $h_m \approx 0.00049$, which is well below $\delta x = \delta y = 0.01$. Without using the lubrication solution, it would have required a significant grid-size reduction that would render the computation infeasible.

Comparing the results for $Re = 100$ and $Re = 10$, we note that the lubrication effect acts at a much smaller gap size in the higher Re case, and it is accompanied by a sharper deceleration. Fig. 16 shows the corresponding vorticity fields in the two cases.

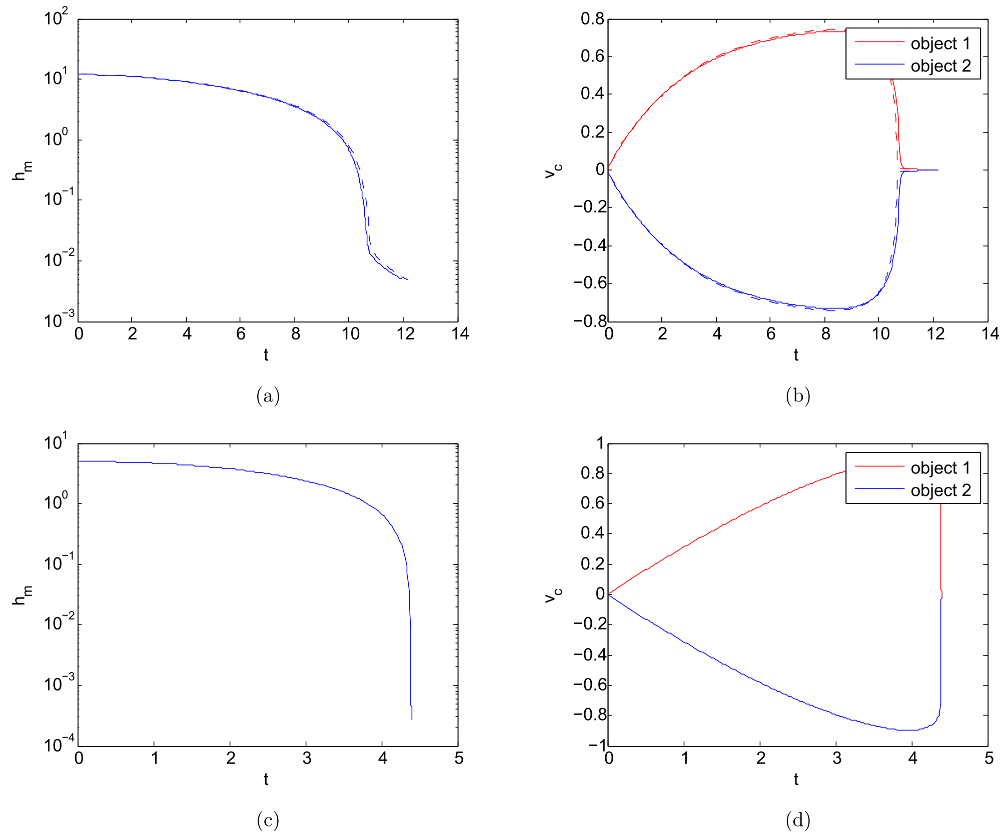

Fig. 15. Minimum gap height h_m and vertical velocity v_c at $Re = 10$ (a,b) and $Re = 100$ (c,d). Two resolutions are used in the case for $Re = 10$, $\delta x = \delta y = 1/80$ (solid lines) and $\delta x = \delta y = 1/40$ (dashed lines). In the case of $Re = 100$, the resolution is $\delta x = \delta y = 1/100$. At $Re = 10$, the lubrication approximations were triggered at $t \approx 10.67$ for $\delta x = \delta y = 1/40$ and at $t \approx 10.48$ for $\delta x = \delta y = 1/80$. At $Re = 100$, the lubrication approximations were triggered at $t \approx 4.35$.

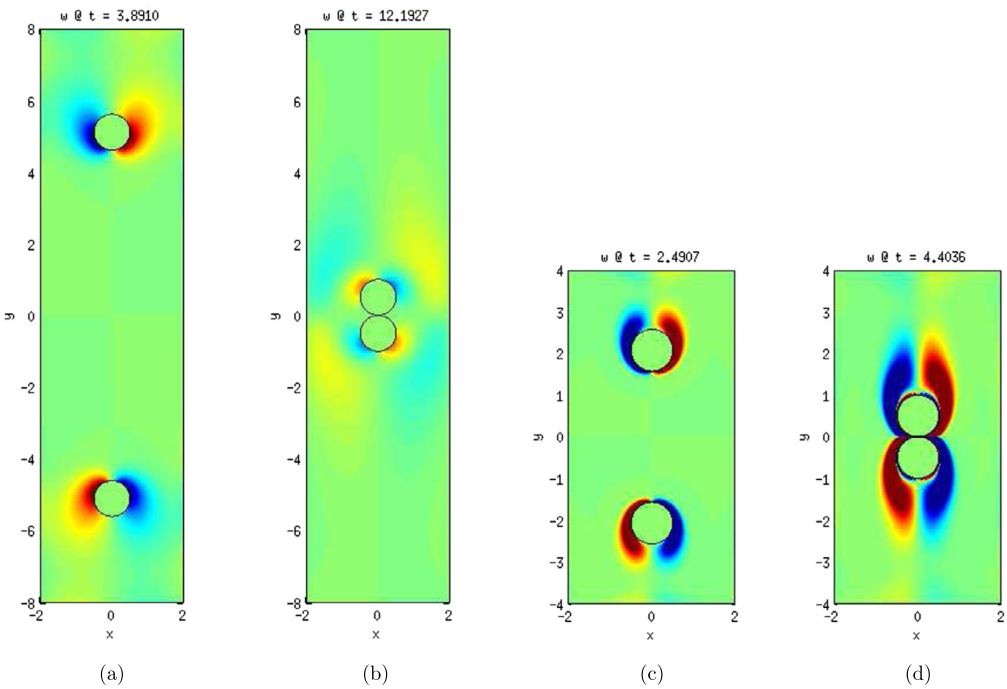

Fig. 16. The vorticity fields plotted using the contours of $sign(\omega)\ln(1 + |\omega|)$. $Re = 10$: (a) before and (b) after the lubrication approximations were triggered. $Re = 100$: (c) before and (d) after the lubrication approximations were triggered.

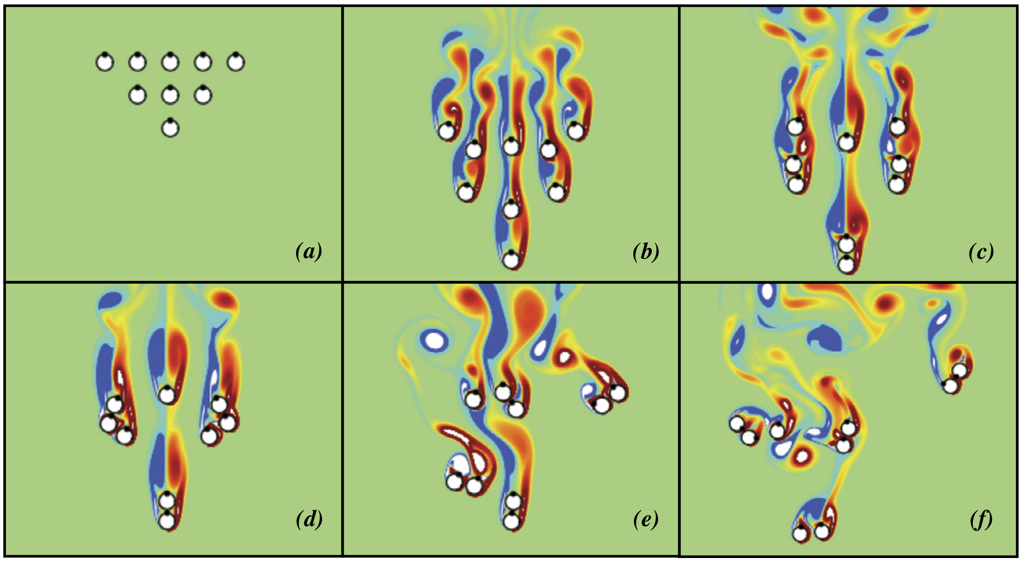

Fig. 17. A lattice of particles settling in a fluid already exhibits the tendency for clustering. In this case it is simulated using a simple dry collision model. It needs the proper treatment of the collision using the new method described in the paper.

The method used in this case can be generalized to compute more complex systems of particle interactions (Fig. 17).

4. Summary and outlook

Motivated by the need and the challenge of computing particle collisions while resolving both the unsteady flows and the dynamics of the particles, we constructed a method that integrates the lubrication solutions into the framework of the immersed interface method for the Navier-Stokes equations. The method works for freely moving particles, and can resolve collision dynamics when the gaps between the particles are arbitrarily small. The method presented here is the first to successfully integrate the two-way coupling between the NS equations with the lubrication equations in order to compute particle collisions in a fluid.

Declaration of competing interest

The authors declare that they have no known competing financial interests or personal relationships that could have appeared to influence the work reported in this paper.

Acknowledgements

Author contributions: AY, SX, and ZJW worked on the initial submission. SX and ZJW worked on the final version, which expands the method to the general cases and also provides additional numerical tests. SX thanks NSF for the support of his work on the immersed interface method under the grant NSF DMS 1320317.

References

[1] A. El Yacoubi, S. Xu, Z.J. Wang, Computational study of the interaction of freely moving particles at intermediate Reynolds numbers, J. Fluid Mech. 705 (2012) 134–158.
[2] A. El Yacoubi, S. Xu, Z.J. Wang, The effect of gravity and dimensionality on the impact of cylinders and spheres onto a wall in a viscous fluid, Phys. Fluids 29 (2017) 020717.
[3] D.J. Jeffrey, Y. Onishi, The slow motion of a cylinder next to a plane wall, Q. J. Mech. Appl. Math. XXXIV, Pt. 2 (1981) 129–137.
[4] R.J. LeVeque, Z. Li, The immersed interface method for elliptic equations with discontinuous coefficients and singular sources, SIAM J. Numer. Anal. 31 (4) (1994) 1019–1044.
[5] Z. Li, K. Ito, The Immersed Interface Method: Numerical Solutions of PDEs Involving Interfaces and Irregular Domains, Frontiers in Applied Mathematics, vol. 33, SIAM, 2006.
[6] C. Peskin, The immersed boundary method, Acta Numer. 11 (2002) 479–517.
[7] O. Reynolds, On the theory of lubrication and its application to Mr Beauchamp Tower's experiments, including an experimental determination of the viscosity of olive oil, Philos. Trans. R. Soc. Lond. A 177 (1886) 228–310.
[8] S. Xu, Z.J. Wang, An immersed interface method for simulating the interaction of a fluid with moving boundaries, J. Comput. Phys. 216 (2006) 454–493.
[9] S. Xu, Z.J. Wang, Systematic derivation of jump conditions for the immersed interface method in three-dimensional flow simulation, SIAM J. Sci. Comput. 27 (6) (2006) 1948–1980.
[10] S. Xu, Z.J. Wang, A 3D immersed interface method for fluid-solid interaction, Comput. Methods Appl. Mech. Eng. 197 (2008) 25–28.

[11] S. Xu, The immersed interface method for simulating prescribed motion of rigid objects in an incompressible viscous flow, J. Comput. Phys. 227 (2008) 5045–5071.

[12] S. Xu, Singular forces in the immersed interface method for rigid objects in 3D, Appl. Math. Lett. 22 (2009) 827–833.

[13] S. Xu, A boundary condition capturing immersed interface method for 3D rigid objects in a flow, J. Comput. Phys. 230 (2011) 7176–7190.

[14] S. Xu, G.D. Pearson, Computing jump conditions for the immersed interface method using triangular meshes, J. Comput. Phys. 302 (2015) 59–67.